JVST A
Journal of Vacuum Science & Technology A

Heterovalent semiconductor structures and devices grown by molecular beam epitaxy

Cite as: J. Vac. Sci. Technol. A **39**, 030803 (2021); https://doi.org/10.1116/6.0000802
Submitted: 20 November 2020 • Accepted: 05 March 2021 • Published Online: 01 April 2021

Yong-Hang Zhang and David J. Smith

JVST A
Journal of Vacuum Science & Technology A

REVIEW

avs.scitation.org/journal/jva

Heterovalent semiconductor structures and devices grown by molecular beam epitaxy

Cite as: J. Vac. Sci. Technol. A **39**, 030803 (2021); doi: 10.1116/6.0000802
Submitted: 20 November 2020 · Accepted: 5 March 2021 ·
Published Online: 1 April 2021

Yong-Hang Zhang[1,a)] and David J. Smith[2]

AFFILIATIONS

[1]School of Electrical, Computer and Energy Engineering, Arizona State University, Tempe, Arizona 85287
[2]Department of Physics, Arizona State University, Tempe, Arizona 85287

Note: This paper is part of the Special Topic Collection: Honoring Dr. Art Gossard's 85th Birthday and his Leadership in the Science and Technology of Molecular Beam Epitaxy.

[a)]**Author to whom correspondence should be addressed:** yhzhang@asu.edu

ABSTRACT

Heterovalent structures consisting of group II-VI/group III-V compound semiconductors offer attractive properties, such as a very broad range of bandgaps, large conduction band offsets, high electron and hole mobilities, and quantum-material properties such as electric-field-induced topological insulator states. These properties and characteristics are highly desirable for many electronic and optoelectronic devices as well as potential condensed-matter quantum-physics applications. Here, we provide an overview of our recent studies of the MBE growth and characterization of zincblende II-VI/III-V heterostructures as well as several novel device applications based on different sets of these materials. By combining materials with small lattice mismatch, such as ZnTe/GaSb ($\Delta a/a \sim 0.13\%$), CdTe/InSb ($\Delta a/a \sim 0.05\%$), and ZnSe/GaAs ($\Delta a/a \sim 0.26\%$), epitaxial films of excellent crystallinity were grown once the growth conditions had been optimized. Cross-sectional observations using conventional and atomic-resolution electron microscopy revealed coherent interfaces and close to defect-free heterostructures. Measurements across CdTe/InSb interfaces indicated a limited amount (~1.5 nm) of chemical intermixing. Results for ZnTe/GaSb distributed Bragg reflectors, CdTe/$Mg_xCd_{1-x}Te$ double heterostructures, and CdTe/InSb two-color photodetectors are briefly presented, and the growth of a rock salt/zincblende PbTe/CdTe/InSb heterostructure is also described.

I. INTRODUCTION

The concepts of heterostructures[1] and artificial superlattices[2] have created a vast panorama for semiconductor physics featuring novel low-dimensional phenomena, such as quantum confinement, Bloch oscillations,[3] and the fractional quantum Hall effect.[4,5] These developments were enabled by the emergence of molecular beam epitaxy (MBE),[6] and they have also spurred the invention of many novel types of electronic devices, such as high electron mobility transistors,[7] quantum cascade lasers (QCLs),[8] type-II superlattice infrared (IR) photodetectors,[9] and quantum-well IR photodetectors (QWIPs).[10] These devices invariably feature heterojunctions consisting of materials that are both isostructural and isovalent, such as groups IV/IV (Si/Ge), groups III-V/III-V (GaAs/AlAs, GaAs/InAs, InN/GaN), or groups II-VI/II-VI (CdTe/HgTe). In practice, functional devices based on these material combinations are highly sensitive to the presence of structural defects such as misfit and threading dislocations, which are difficult to avoid under normal growth conditions with lattice-mismatched substrates. Hence, the choice of materials combinations and their electronic properties, such as bandgaps, band offsets, effective masses, absorption coefficients, and refractive indices, are often limited, especially for cases involving monolithic integration on (almost) lattice-matched substrates.

A highly attractive, alternative approach is based on the heterogeneous integration of II-VI with III-V compound semiconductors[11] and potentially provides enormous freedom for growing heterovalent structures, such as quantum wells, quantum wires, and quantum dots, which can also be monolithically integrated. The possible II-VI/III-V combinations display an array of novel electronic properties, many of which are markedly different from those provided by the well-known isovalent heterostructures. The wide

range of potential configurations literally represents a combinatorial explosion of options for novel device designs. Moreover, these options could be significantly expanded by growing layers consisting of alternating II-VI or III-V semiconductors. For example, it has recently been theoretically predicted that topological structures could be grown from nontopological components using layered superlattice structures, with a large built-in electric field arising from the charge mismatch between the components at the heterovalent interface.[12] In these proposed heterovalent superlattices, two narrow-gap semiconductors with different valence states would be combined to create a heterovalent heterostructure, such as a CdTe/InSb superlattice.[12] This theoretical prediction of topological insulator properties among common binary octet semiconductors introduces this technologically well-studied group into the realm of topological physics. Meanwhile, there have only been limited reports of practical devices consisting of II-VI/III-V heterojunctions, multiple quantum wells, and superlattices.[13] Research in this direction has recently been expanded to other device applications, such as QCLs and QWIPs on InP[14,15] and optical modulators using ZnTe on Si or sapphire.[16]

Our recent research has been directed toward heterostructures that combine members of the II-VI family (BeMgZnCd)(SeTe) and the III-V family (AlGaIn)(NPAsSbBi), which can be grown on many commercially available semiconductor substrates, such as GaN, Si, Ge, GaAs, InP, InAs, GaSb, and InSb. As illustrated in Fig. 1, these materials (including type-II superlattices) have bandgaps that span the entire wavelength spectrum from far-infrared to near-ultraviolet. This platform of heterovalent materials provides extra capabilities that are not achievable with the conventional families of isovalent heterojunctions. Thus, the II-VI/III-V family offers enormous flexibility to grow different heterovalent alloys, quantum wells, and superlattices, which would provide very interesting physical properties that differ from those of the isovalent heterostructures. Moreover, there are several combinations of II-VI/III-V materials that have the same zincblende crystal structure and are also closely lattice-matched, so that the formation of interfacial misfit dislocations, when initiating growth, should be minimized. These can be roughly separated into four groupings, namely (i) 5.7-Å materials based on GaAs, (ii) 5.9-Å materials based on InP, (iii) 6.1-Å materials based on either GaSb or InAs, and (iv) 6.5-Å materials based on InSb. Importantly, all of these materials have direct bandgaps, which is an essential requirement for optoelectronic devices. In this paper, we provide an overview of our recent research, which has been directed toward the growth and characterization of these lattice-matched families of II-VI/III-V heterostructures, as well as exploring several related device applications.

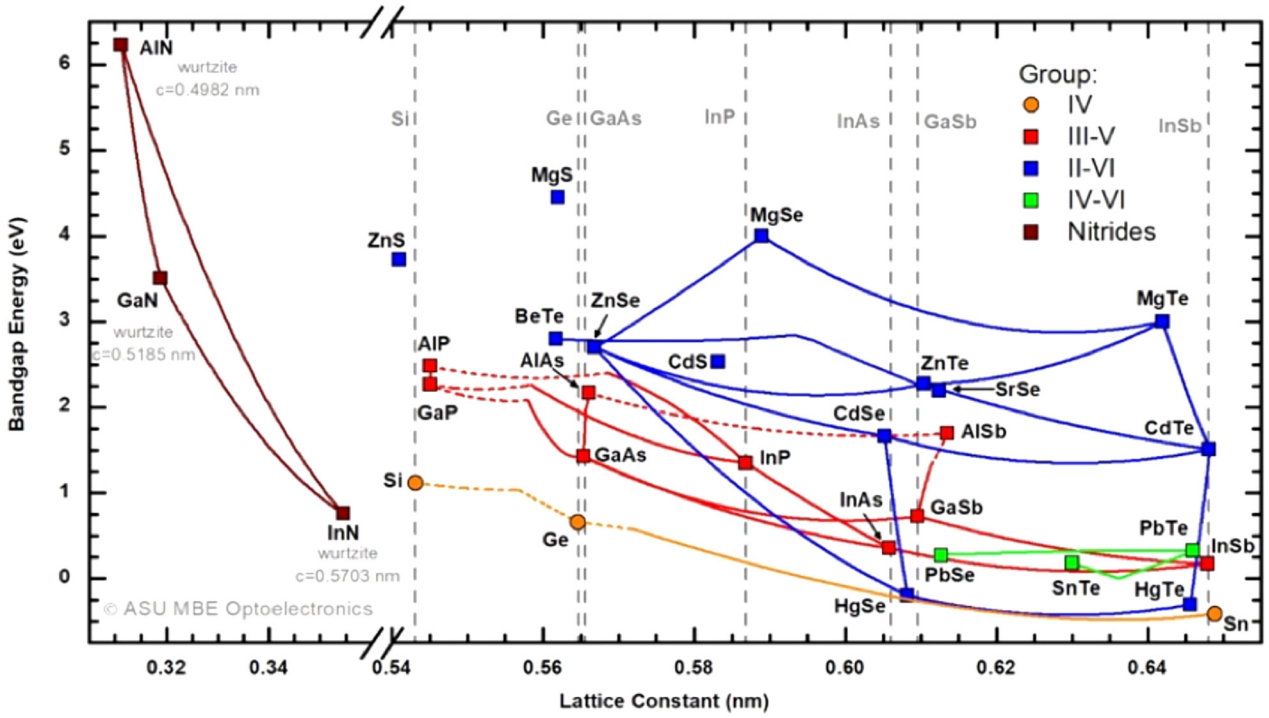

FIG. 1. Plot of bandgap energies for group II-VI (BeMgZnCdHg)(SeTe), group IV-IV (SiGeSnPb), group III-V (AlGaIn)(NPAsSbBi), and group IV-VI (SnPb)(SeTe) binary semiconductors vs lattice constant. The lines connecting binaries represent bandgap energies and lattice constants of different ternary alloys. Solid lines represent direct bandgap alloys, while dashed lines are indirect bandgap alloys.

II. EXPERIMENT

A. MBE growth

Molecular beam epitaxy has been used to grow isovalent II-VI heterostructures for many years. However, these II-VI structures were typically grown on III-V semiconductor substrates such as GaAs, InP, and GaSb, because of the high cost and limited availability of II-VI semiconductor substrates. A strong motivation for the research done prior to the early 1990s was the fabrication of blue laser diodes and light-emitting diodes based on the ZnCdSe/ZnSSe/ZnMgSSe family that was closely lattice-matched to ZnSe or GaAs. Much of the early pioneering research in this area prior to the 1990s has been summarized in a comprehensive review article.[17] The growth of II-VI materials is generally very different from that of III-V materials: (1) The growth temperature is typically much lower than that for III-V materials because of the higher vapor pressures of group-II and group-IV elements. Thus, special precautions need to be taken during any subsequent III-V growth to mitigate against sublimation from the surface of the II-VI material, such as a graded transition layer while ramping up or ramping down the growth temperature. (2) The growth can be carried out under both group-II rich and group-VI rich conditions, which allows for accurate calibration of both group-II and group-VI growth rates using RHEED oscillations.

Two separate MBE systems were used for growing most of the II-VI/III-V heterovalent structures described here: details of the specific growth conditions are given later in Secs. III A–III C. The dual-chamber VG-V80 MBE system, shown in Fig. 2, consists of separate II-VI and III-V growth chambers that are connected via an ultrahigh-vacuum transfer module. The III-V chamber enables the growth of material combinations that contain (InGaAl)(PAsSbBi) with Be, Si, and Te dopants, while the II-VI chamber enables growth of material combinations consisting of (BeMgZnCd)(SeTe) with Al, Ga, In, P, and Bi dopants. Valved graphite effusion cells are used for many of the group-V and group-VI elements. These cells have specially designed conical inserts that provide control of flux during growth, and the valves can also be closed completely during growth. Such a design also enables high temperature (~200 °C) bakeout of the II-VI chamber by keeping the valves closed to greatly reduce the residual background pressure inside the growth chamber and results in low background impurity levels in the epilayers.

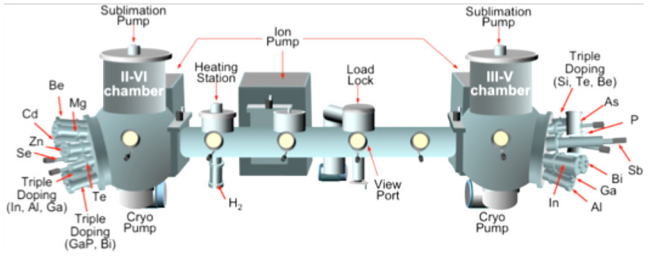

FIG. 2. Diagram illustrating the major features of the dual-chamber MBE system.

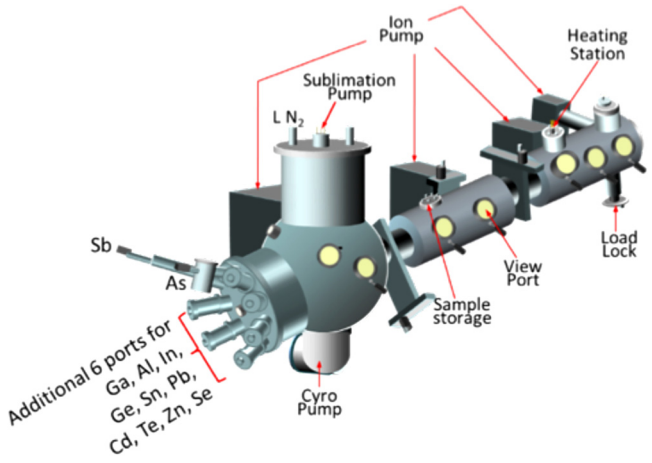

FIG. 3. Schematic showing the single-chamber MBE system and its flexible arrangement of effusion cells.

The single VG-V80 MBE system, as shown in Fig. 3, permits rapid installation of different source combinations containing group-II, III, IV, V, and VI materials in a total of eight ports. This flexible arrangement allows heterovalent quantum structures, including superlattices, to be grown with almost any desired combination of II-VI, III-V, V-VI, and IV-VI compounds. The available source materials include Be, Zn, Cd, B, Al, Ga, In, Ge, Sn, Pb, N, As, Sb, Bi, Se, and Te.

These two MBE systems both incorporate facilities for *in situ* growth monitoring, including reflection high-energy electron diffraction (RHEED) to monitor growth rates and surface reconstruction, residual gas analyzers to analyze the background vacuum, diffuse reflectance spectroscopy for accurate measurement of substrate temperature, and two pyrometers suitable for different temperature ranges.

B. Characterization

Several *ex situ* techniques were used to characterize the structural and optical properties of the II-VI/III-V heterostructures after completion of MBE growth. X-ray diffraction measurements were made using a PANalytical X'Pert PRO Materials Research Diffractometer equipped with a triple-axis module and a Cu K-α source. Photoluminescence spectra for ZnTe/GaSb heterostructures were recorded using a Nicolet Magna-IR 760 Fourier Transform Infrared Spectrometer, while a SPEX 1404 double-grating spectrometer was used with the ZnSe/GaAs samples. Cross sections of the II-VI/III-V heterostructures were prepared for observation by transmission electron microscopy (TEM) using conventional mechanical polishing followed by argon-ion-milling at low energy (~2 keV) with the sample maintained at liquid-nitrogen temperature to minimize any ion-beam-induced artifacts.[18] All samples were sliced to enable TEM imaging with a [110]-type crystal projection aligned parallel to the incident electron beam direction. Standard TEM studies used a Philips-FEI CM200 FEG TEM operated at 200 keV, high-resolution TEM imaging used a JEM-4000EX

operated at 400 keV, and aberration-corrected imaging was done with a probe-corrected JEM ARM200F operated at 200 keV.

III. RESULTS

A. ZnTe/GaSb

1. Growth

The oxide layers on undoped GaSb (100) substrates were first thermally desorbed at 500 °C in the III-V chamber under Sb flux with a beam equivalent pressure (BEP) of $\sim 1.6 \times 10^{-6}$ Torr, followed by growth of a thin (~20 nm) GaSb buffer layer at 480 °C using a dual-chamber MBE system in Furdyna's group at Notre Dame University, with similar cell configurations as shown in Fig. 2.[19] The substrate temperatures were usually measured using a thermocouple on the back of the substrate holder, which had been previously calibrated using a pyrometer. The samples were then cooled down to room temperature and transferred to the II-VI chamber. The ZnTe growth was initialized under Zn flux for several seconds prior to opening the Te shutter in order to minimize the possible formation of any Ga_2Te_3 phase.[20,21] The substrate temperatures were typically varied between 300 and 350 °C and the BEP ratios of Zn to Te were adjusted to optimize the growth conditions.[18]

During the ZnTe growth, the surface reconstructions were monitored *in situ* using RHEED. The typical (1×3) pattern of the GaSb surface was clearly visible before initiation of the ZnTe layer growth. Initially, the RHEED diffraction spots appeared spotty and weakly defined, indicating a transition from a (1×3) surface to a (1×2) surface. This transition usually took place in as little as 10 s and was attributed to the formation of a thin ill-defined layer between ZnTe and GaSb. After this transition period, the (1×2) ZnTe surface reconstruction pattern started to appear, and a bright and streaky pattern with a clear (1×2) reconstruction was visible for the remainder of the ZnTe growth.

2. Characterization

After completion of growth, high-resolution XRD measurements were performed in the vicinity of the (004) GaSb diffraction peak. As shown in Fig. 4(a), the XRD ω-2θ pattern from a single ZnTe layer (nominal thickness of 110 nm) revealed distinct peaks for the GaSb substrate and the ZnTe layer. Pendellösung fringes were clearly visible, confirming that the epitaxial film was highly crystalline with smooth interfaces, uniform thickness, and low defect density. The simulated ω-2θ curve, also shown in Fig. 4(a), indicated a film thickness of ~105 nm and strain relaxation of ~30%. Cross-sectional TEM observations confirmed the excellent sample crystallinity. The high-resolution image shown in Fig. 4(b) indicates a very smooth, barely perceptible ZnTe/GaSb interface. Thus, exposure of GaSb to the Zn flux prior to the ZnTe growth must significantly suppress any Ga_2Te_3 layer formation at the interface, unlike previous reports.[22] Moreover, no interfacial misfit dislocations and stacking faults were observed across many micrometers of the ZnTe/GaSb heterostructure, indicating that a nearly defect-free interface between ZnTe/GaSb had been achieved as a result of the very small lattice mismatch. Further atomic-resolution images of other ZnTe/III-V heterostructures showing increasing defect densities due to larger lattice mismatch can be found elsewhere.[23]

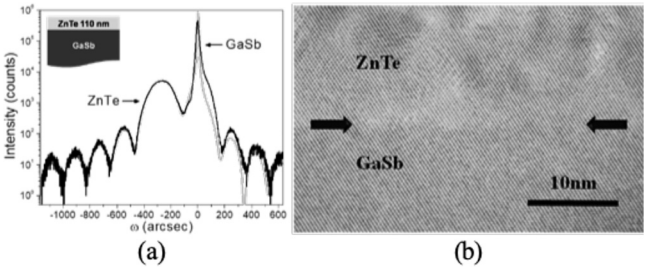

FIG. 4. (a) High-resolution XRD patterns of ω-2θ (004) diffraction measurements of single 110-nm-thick ZnTe layer grown on GaSb(100) substrate. Measured data are shown in black and simulation results are shown in gray. (b) TEM image of the same ZnTe layer sample, with arrows pointing to ZnTe/GaSb interface. Reprinted with permission from Wang *et al.*, J. Cryst. Growth **311**, 2116 (2009). Copyright 2009, Elesvier.

Resolution improvements to better than 1.0 Å as provided by aberration-corrected TEMs make it possible to resolve individual atomic columns ("dumbbells") when imaging compound semiconductors in [110]-type projections.[24] Figure 5 shows a pair of atomically resolved images of a heterovalent ZnTe/GaSb(001) interface: this particular sample was grown in the dual-chamber MBE at the Notre Dame University, also equipped with an interlock exchange for UHV sample transfer.[25] Because of the close similarity in atomic numbers of the four constituent elements, the approximate interface location, indicated here by arrows, is difficult to locate by direct visual inspection.

3. GaSb/ZnTe distributed Bragg reflectors

Midwave infrared (MWIR) laser diodes have attracted much interest because of their potential applications in chemical sensing and spectroscopy in the spectral range from 2 to 5 μm. Compact single-mode vertical-cavity surface-emitting lasers (VCSELs) with

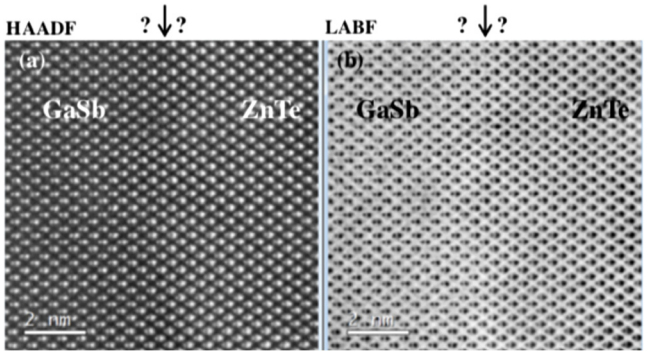

FIG. 5. Aberration-corrected atomic-structure images of the ZnTe/GaSb interface. Approximate location of the interface is indicated by arrows. (a) High-angle annular-dark-field image; (b) large-angle bright-field image. Reprinted with permission Smith, Prog. Cryst. Growth Char. Mater. **66**, 100498 (2020). Copyright 2020, Elsevier.

narrow spectral linewidth is ideal for such applications. One of the key structures used in a VCSEL is a high reflectivity mirror, usually in the form of distributed Bragg reflectors (DBRs). However, most isovalent III-V compound semiconductor pairs for DBRs that are closely lattice-matched to InP or GaSb substrates have very small refractive index contrast, making it difficult to achieve high reflectivity and low series resistance to reduce the VCSEL threshold current density.

The lattice mismatch between ZnTe and GaSb is only ~0.13%, which allows for monolithic integration of DBR structure using heterovalent ZnTe/GaSb pairs with other GaSb-based materials without resulting in substantial misfit dislocations. Moreover, GaSb and ZnTe have large refractive index contrast in the MWIR range (for example, $\Delta n = 1.18$ at 0.6 eV), which is significantly larger than for other III-V semiconductor isovalent pairs often used in MWIR DBRs.[26]

A series of ZnTe/GaSb DBR samples with different numbers of λ/4 pairs was grown using a dual-chamber MBE system described above. The DBR structures were grown on a GaSb (001) substrate with an unintentionally doped GaSb buffer layer. During the growth, ZnTe epilayers were deposited at 320 °C in the II-VI chamber, while GaSb epilayers were grown in the III-V chamber using a temperature ramp method to protect the ZnTe layer surfaces and to achieve high material quality. The wafer was transferred between II-VI and III-V chamber repeatedly to complete the whole DBR structure. The detailed growth conditions were reported in Refs. 25 and 26.

Figure 6(a) shows the cross-sectional image of a seven-pair ZnTe/GaSb DBR sample taken in this case with a scanning electron microscope. The bright regions correspond to ZnTe and the dark regions to GaSb. The ZnTe and GaSb layer thicknesses were determined to be $d_{ZnTe} = 231 \pm 10$ nm and $d_{GaSb} = 165 \pm 10$ nm, respectively, in close agreement with estimates based on MBE growth rates. Cross-sectional TEM images for several of the ZnTe/GaSb DBR samples indicated high quality ZnTe and GaSb epilayers with low defect density, and smooth, defect-free ZnTe/GaSb and GaSb/ZnTe interfaces. The optical reflectance spectrometry measurements shown in Fig. 6(b) indicate a peak reflectivity of 99.0% with a wide stopband of 480 nm centered at 2.5 μm. Furthermore, comparison of the simulated reflectance spectrum with the experimental data reveals excellent agreement in terms of peak reflectivity

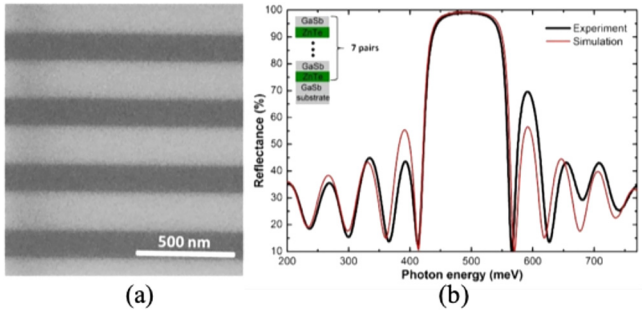

FIG. 6. (a) Cross-sectional SEM image, and (b) measured and simulated reflectance spectra for ZnTe/GaSb DBR sample. Reprinted with permission Fan *et al.*, Appl. Phys. Lett. **101**, 121909 (2012). Copyright 2012, AIP Publishing LLC.

(99.3%), bandwidth of photonic stopband (481 nm), and sidelobe positions.[26]

B. CdTe/InSb

1. Growth

The growth of CdTe on InSb(001) substrates started with oxide removal from the InSb substrate surface. The process heated up the substrate at a slow rate of 5 °C/min up to a pyrometer reading of 475–480 °C, with 3-min pause after each temperature ramp to prevent the substrate from overheating. The reason for the carefully controlled temperature change is because the temperature for InSb oxide removal is close to the InSb melting point. The substrates were kept at this temperature for 1 h, and completion of oxide removal was confirmed by observation of a streaky pseudo-(1 × 3) RHEED pattern. While the substrate temperature was being ramped, streaky RHEED patterns appeared at $T_{sub} \sim 424$ °C and then became spotty as the temperature was further ramped to about 460 °C. This phenomenon corresponds to a two-stage surface oxide removal, first of Sb_2O_5 and then of In_2O_3. Finally, streaky pseudo-(1 × 3) and c(4 × 4) patterns were observed, representing the oxide-free InSb surface.[27,28]

After oxide removal, the substrate temperatures were normally reduced to 390 °C for growth of a 500-nm-thick InSb buffer layer, with a growth rate of 10.8 nm/min and an Sb/In flux ratio of 1.5. The samples were then transferred under UHV conditions to the II-VI chamber. Streaky RHEED patterns confirmed that the surfaces had retained their high quality after the sample transfer. Before commencement of CdTe growth, the InSb surface was exposed to a Cd flux for several minutes to prevent formation of any interfacial III-VI alloy compound. Meanwhile, the RHEED pattern typically changed to a (3 × 2) reconstruction. A CdTe buffer layer was then grown using an initial Cd/Te flux ratio of 3.0, which was reduced to 1.5 after 2 min of growth. The RHEED pattern became slightly hazy upon initiation of the CdTe growth, as the surface reconstruction transitioned from InSb to CdTe, and then became streaky after ~10 min of growth. Clear (2 × 1) and c(2 × 2) RHEED reconstruction streaks were observed indicating Cd-rich growth conditions. The initial substrate temperature prior to growth was usually set to 280 °C (pyrometer reading), and the temperature was gradually decreased to ~265 °C as the II-VI layers were deposited due to the change in emissivity of the wafer surface.[27,28]

2. Characterization

Figure 7(a) shows the typical ω-2θ (004) XRD pattern for a single CdTe layer grown on an InSb(001) substrate.[27,28] The FWHMs of the InSb substrate and the CdTe peaks are 22 and 17 arcsecs, respectively. High-resolution TEM imaging, as shown by the example in Fig. 7(b), further reveals the very low defect densities and excellent crystallinity of the epitaxial CdTe films.[29] Monochromatic x-ray photoemission spectroscopy and ultraviolet photoemission spectroscopy were used to characterize the electronic states of the clean InSb and CdTe surfaces, as well as the CdTe/InSb (001) heterojunctions. In this case, a remote hydrogen-plasma process was used at room temperature to clean the surfaces prior to characterization. As shown in Fig. 7(c), the results

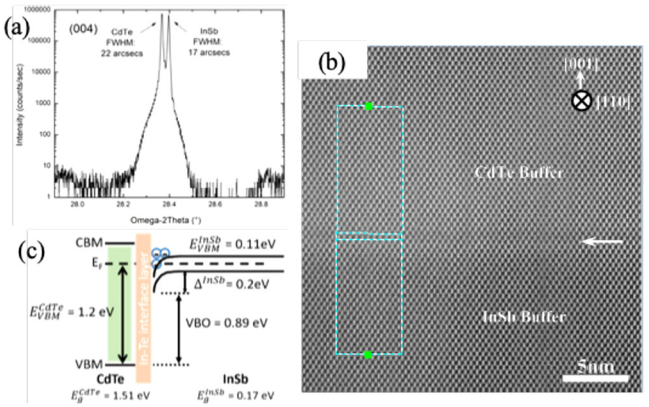

FIG. 7. (a) ω-2θ (004) XRD pattern of CdTe/InSb heterostructure on the InSb substrate (Ref. 28). The FWHMs of the InSb substrate and the CdTe peaks are 22 and 17 arcsecs, respectively. (b) High-resolution TEM image showing a highly ordered interface between CdTe and InSb (Ref. 29). (c) Schematic diagram of band alignment of a CdTe/InSb(001) heterojunction. Reprinted with permission Wang *et al.*, J. Vac. Sci. Technol. A **36**, 031101 (2018). Copyright 2018, AIP Publishing LLC.

indicated a valence band offset of 0.89 eV and a type-I alignment at the heterovalent CdTe/InSb heterostructure interface.[30]

3. Heterocrystalline PbTe/CdTe/InSb structure

The rock salt chalcogenides are generating much current attention, especially because of their potential applications as quantum materials, as well as for infrared lasers and photodetectors. Rock salt PbTe has a unit-cell lattice parameter ($a = 6.462$ Å) that is very close to those of zincblende CdTe and InSb (see Fig. 1). The closely coincident nature of these three lattice constants has motivated our recent interest in exploring the use of CdTe/InSb heterostructures as composite substrates for PbTe growth.[31] Experiments with different flux conditions indicated that using a Te overpressure for a period of 60 s led to a smooth transition between the zincblende CdTe and the rock salt PbTe. Streaky (1×1) RHEED patterns indicated the layer-by-layer PbTe growth. Cross-sectional TEM observations showed the high crystalline quality of the PbTe epilayer and the absence of interfacial dislocations, while the aberration-corrected dark-field and bright-field images in Fig. 8 confirm the abruptness of the PbTe/CdTe interface and clearly show the [001] || [001] vertical lattice-plane alignment.

4. CdTe/InSb interfacial intermixing

The actual composition profiles prevailing across the heterovalent CdTe/InSb interface is an important issue, especially considering the theoretical predictions of charge accumulation arising from the valence mismatch. A compilation of interface abruptness values indicates that a minimum attainable width, attributed to island-mediated growth, is applicable to a range of isovalent, isostructural heterostructures.[32] More recent studies of noncommon-atom isovalent InAs/GaSb superlattices using aberration-corrected structure

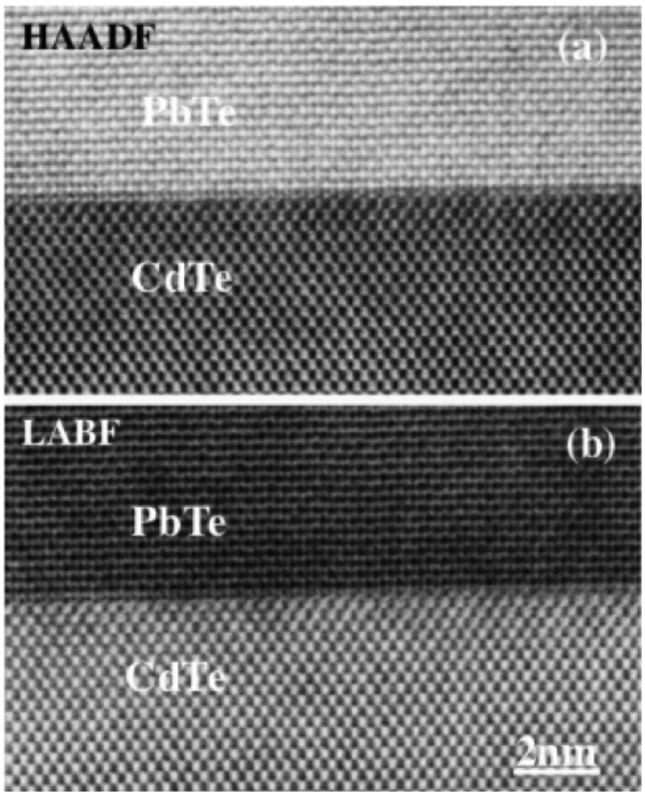

FIG. 8. Aberration-corrected atomic-structure images showing an abrupt PbTe/CdTe interface, with [001] || [001] vertical lattice-plane alignment and absence of interfacial dislocations: (a) High-angle annular-dark-field; (b) large-angle bright-field. Reprinted with permission Lassise *et al.*, J. Appl. Phys. **126**, 045708 (2019). Copyright 2019, AIP Publishing LLC.

imaging showed a similar trend.[33] Our detailed observations of the heterovalent CdTe/InSb interface followed the same pattern.[34] Measurements of interface intensity profiles were made using both aberration-corrected atomic-structure imaging and chemically sensitive $\boldsymbol{g_{002}}$ dark-field (DF) imaging. The former were limited in accuracy because of the extreme closeness of the lattice parameters and also because of the closeness in atomic numbers of the four elements involved, i.e., Cd(48), Te(52), In(49), and Sb(51). Conversely, as clearly apparent from the micrographs shown in Fig. 9, the interface is readily visible in DF images. Matching between simulated and experimental intensity profiles revealed an interface width of ~1.5 nm (10%–90% criterion).[34] Similar trends in chemical intermixing are also expected across interfaces between other II-VI-III-V combinations.[24]

5. CdTe/$Mg_xCd_{1-x}Te$ double heterostructure

Double heterostructures consisting of CdTe/$Mg_xCd_{1-x}Te$ have much potential for solar cell and near-infrared photodetector applications. The extremely small lattice-mismatches between InSb and both CdTe and MgTe (0.03% and 0.09%, respectively) enable a

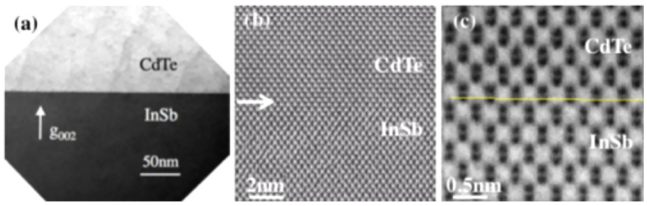

FIG. 9. Comparison of electron micrographs of CdTe/InSb interface for several different imaging modes: (a) ***g002*** dark-field image; (b) high-resolution lattice image; (c) aberration-corrected large-angle bright-field image. Reprinted with permission Smith, Prog. Cryst. Growth Char. Mater. **66**, 100498 (2020). Copyright 2020, Elsevier.

high degree of structural perfection with very low defect densities, which are highly desirable for minority carrier device applications. Moreover, the double heterostructure designs offer optimal confinement for minority carriers as well as excellent passivation of the surfaces of the CdTe absorber layer. A set of CdTe/$Mg_xCd_{1-x}Te$ double heterostructure samples with different CdTe layer thicknesses and $Mg_xCd_{1-x}Te$ barrier heights were grown using MBE. Figure 10 shows a schematic of the layer structure as well as a band edge diagram. The purpose of these wider-bandgap $Mg_xCd_{1-x}Te$ barriers was effectively to confine the minority carriers to the narrower-bandgap CdTe layers. Moreover, the CdTe and $Mg_xCd_{1-x}Te$ are closely lattice-matched so that the interfaces should be close to ideal with few defects, which should minimize any interfacial recombination.[27–28,35–37]

Carrier lifetimes were measured for samples with different CdTe layer thicknesses and $Mg_xCd_{1-x}Te$ barrier configurations using time-resolved photoluminescence (TRPL). Figure 11(a) shows TRPL results for a set of four CdTe/$Mg_xCd_{1-x}Te$ samples, each consisting of two 30-nm-thick intrinsic $Mg_{0.46}Cd_{0.54}Te$ barriers and a CdTe middle layer with n-type background doping on the order of 10^{14} cm^{-3} and a thickness between 220 and 541 nm, as determined by HRXRD measurements. All samples exhibited effective carrier lifetimes exceeding 2 μs, as determined by fitting single exponentials to the TRPL decay tails, attesting to the high quality of the CdTe layers and the CdTe/$Mg_xCd_{1-x}Te$ heterointerfaces.[38] The longest lifetime of 3.6 μs was substantially longer than the previous records for crystalline bulk CdTe,[39] and CdTe/$Mg_xCd_{1-x}Te$ double heterostructures,[40,41] and either surpassed or was comparable to the record lifetimes reported for III/V heterostructures, such as GaAs/(Al,Ga)As and $Ga_{0.5}In_{0.5}P$/GaAs/$Ga_{0.5}In_{0.5}P$ double heterostructures grown by organometallic chemical vapor deposition.[42,43]

Further efforts concentrated on factors affecting the effective carrier lifetimes and interface recombination velocities. Figure 11(b) plots inverse nonradiative lifetime ($1/\tau_{non}$) versus inverse CdTe layer thickness ($2/d$) for the four samples shown in Fig. 11(a), which have 30-nm-thick $Mg_{0.46}Cd_{0.54}Te$ barriers, and for another set of four samples with identical layer structure and alloy composition but with 22-nm-thick barriers. Weighted fittings yielded effective interface recombination velocities of 1.2 ± 0.7 and 1.4 ± 0.6 cm/s, which are comparable to or better than the highest

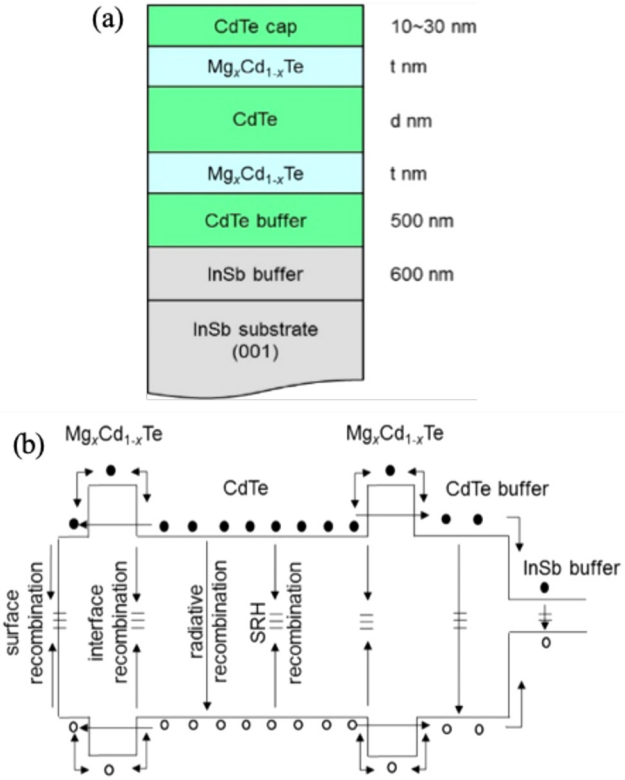

FIG. 10. (a) Sample structure of CdTe/$Mg_xCd_{1-x}Te$ double heterostructures; (b) Schematic band edge alignment for CdTe/$Mg_xCd_{1-x}Te$ double heterostructures and different recombination processes. Reprinted with permission Zhao *et al.*, *Proceedings of the 43rd IEEE PVSC*, Portland, OR, June 5–10, 2015 (IEEE, New York, 2016), pp. 2302–2305. Copyright 2016, IEEE.

values reported for GaAs/$Al_{0.5}Ga_{0.5}As$ (18 cm/s) and GaAs/$Ga_{0.5}In_{0.5}P$ (1.5 cm/s).[42,43]

6. CdTe/InSb two-color photodetectors

Multicolor photodetectors for different IR bands are desirable for sensing and imaging applications, including communications, spectroscopy, autonomous automobiles, and security and environmental monitoring. II-VI/III-V materials that are lattice-matched to InSb substrates are suitable for the visible/midwave-IR spectral range. Optically addressed visible/MWIR two-color photodetectors (2CPDs) using epitaxial CdTe layers grown on lattice-matched InSb layers, with InSb (100) substrates, have been demonstrated with cutoff wavelengths at 77 K of 800 nm and 5.5 μm for CdTe and InSb, respectively.[44–46]

Figure 12(a) shows a schematic of the layer structure of the CdTe-PN junction/InSb-PN junction 2CPD device. After growth of the III-V and II-V semiconductor layers, an 8-nm-thick *p*-type amorphous silicon contact layer with a doping concentration of 1×10^{18} cm^{-3} was deposited using plasma-enhanced CVD. The samples were then annealed at 200 °C in air for 1 min to ensure

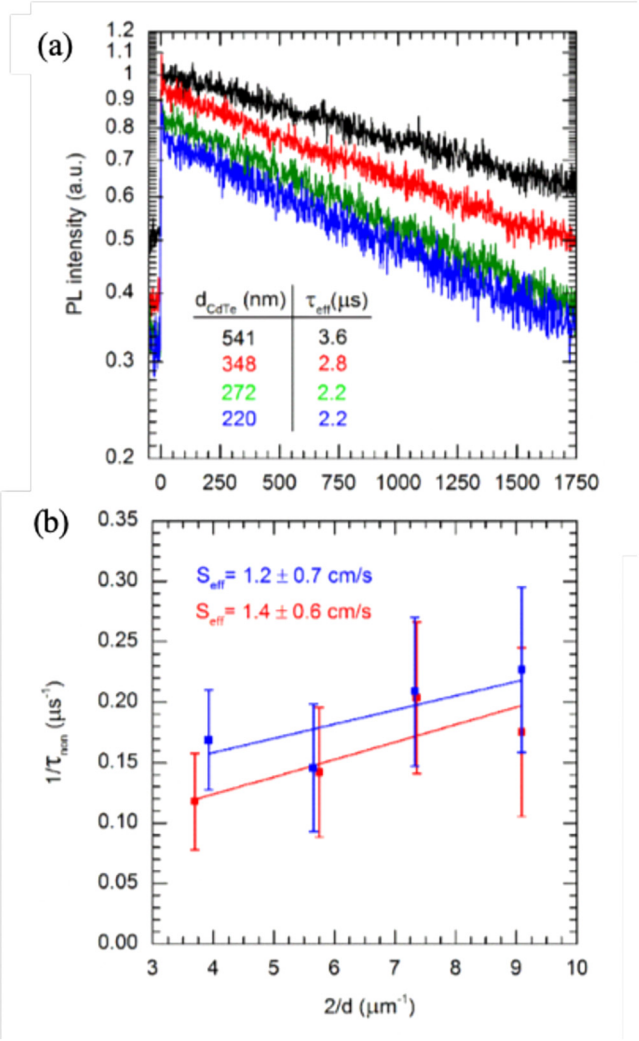

FIG. 11. (a) Normalized room temperature time-resolved photoluminescence decay of four DH samples, each consisting of two 30-nm $Mg_{0.46}Cd_{0.54}Te$ barriers and a CdTe layer with varying thickness. Curves offset along the *y* axis for clarity. Fitted lifetimes are shown together with CdTe layer thicknesses in the table in the inset. (b) Inverse nonradiative recombination lifetime, $1/\tau_{non}$,, vs inverse CdTe layer thickness, $2/d$. The effective interface recombination velocities were extracted by fitting these data. Error bars of $1/\tau_{non}$ were determined by considering uncertainty of estimated radiative lifetimes due to estimation of doping densities. Reprinted with permission Zhao *et al.*, Nat. Energy **1**, 16067 (2016). Copyright 2016, Nature Publishing Group.

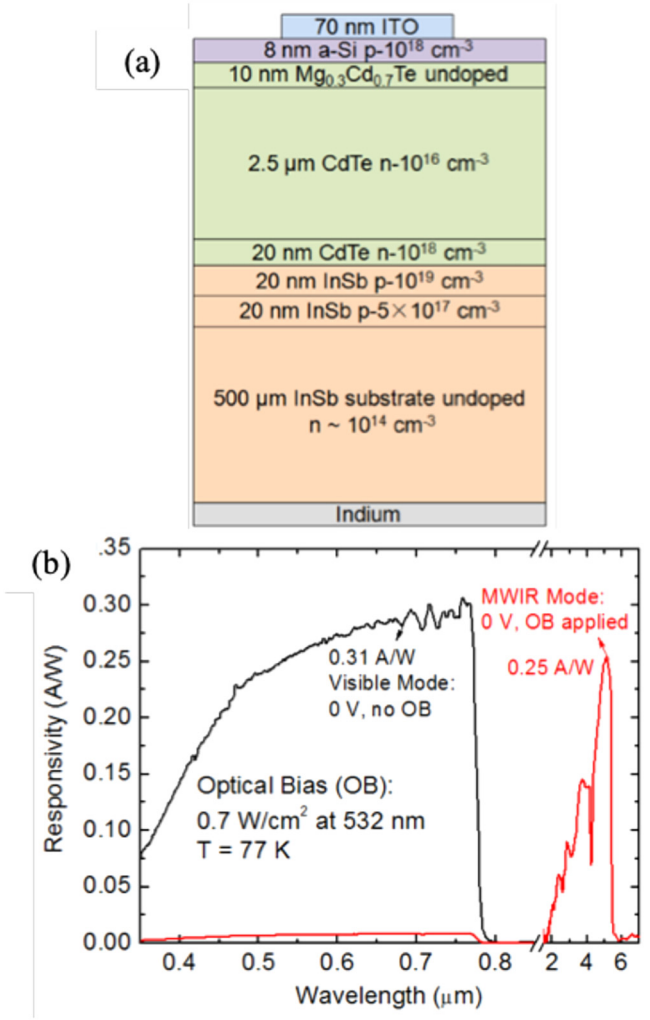

FIG. 12. (a) Layer structure and (b) responsivity of the CdTe-PN junction/InSb-PN junction 2CPD under different optical bias. Reprinted with permission He *et al.*, Infrared Phys. Technol. **97**, 58 (2019). Copyright 2019, Elsevier.

good ohmic In/InSb contacts. The *p*-InSb/*n*-CdTe heterointerfaces had a low resistance of ~0.04 Ω cm^2 at 77 K, as revealed by *I*–*V* measurements of a standalone heterovalent tunnel junction comprised of an *n*-type (10^{18} cm^{-3}) CdTe layer grown on a *p*-type (10^{19} cm^{-3}) InSb layer.[47] Thus, this visible/MWIR 2CPD device design offers the possibility to achieve compact visible/MWIR focal plane arrays with high fill factors. In principle, one could also use the same concept to design monolithically integrated two-terminal photodetectors with more than two detection wavelength bands, which would have even broader applications for satellite remote sensing and environmental monitoring.

C. ZnSe/GaAs

1. Growth

A ZnSe/GaAs double heterostructure sample was grown using the dual-chamber MBE system, starting with a 2-in. *n*-type GaAs (001) substrate, as illustrated by the schematic in Fig. 13(a).[48] The native substrate oxide was first removed with the sample in the III-V chamber under As overpressure at a temperature of 610 °C until a 2 × 4 surface reconstruction was observed with RHEED.

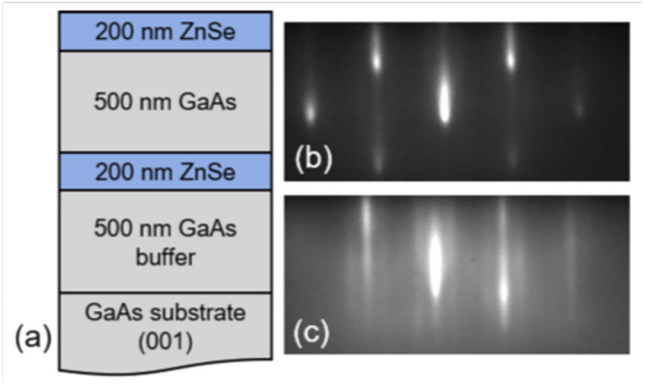

FIG. 13. (a) Schematic illustrating the structure of the ZnSe/GaAs double heterostructure. RHEED patterns at (b) initiation of GaAs growth on ZnSe at 280 °C and (c) after 200 nm of GaAs growth. Reprinted with permission Lassise *et al.*, J. Vac. Sci. Technol. B **36**, 02D110 (2018). Copyright 2018, AIP Publishing LLC.

A 500-nm-thick GaAs buffer layer was then grown at 580 °C at a growth rate of 10 nm/min under an As/Ga flux ratio of 1.5:1. The substrate temperature was ramped down under As overpressure, and the sample was then transferred at room temperature to the II-VI chamber. The substrate temperature was increased to 280 °C before exposure to Zn overpressure to avoid any possible Se–Ga interfacial bonding. The ZnSe deposition began with the application of Se flux with the Se/Zn flux ratio slightly above unity. The RHEED reconstruction immediately transitioned to a streaky 2×1 as the ZnSe growth was initiated, indicating the formation of a smooth interface. After growth of the ZnSe barrier layer, the sample was transferred back to the III-V chamber for GaAs growth. The GaAs layer was initiated by opening the Ga shutter at a substrate temperature of 280 °C after first applying a 3-min As soak at 250 °C. The substrate temperature was then ramped up to 500 °C at a rate of 15 °C/min while the GaAs was being grown at a rate of 10 nm/min. Thus, the growth temperature reached 500 °C after 150 nm of GaAs had grown. The RHEED reconstruction started off spotty at the beginning of the GaAs layer growth at 280 °C but became streaky at a thickness of around 150 nm, as shown in Figs. 13(b) and 13(c), respectively, indicating that a smooth surface had been obtained. The final ZnSe barrier was grown using the same previous method in order to obtain As–Zn bonding configuration at the interface.

2. Characterization

XRD measurements of the ZnSe/GaAs double heterostructure (DH) showed strong peaks from the II-VI and III-V layers, while Pendellösung fringes surrounding the peaks indicated abrupt interfaces. Moreover, excellent crystal quality was retained throughout the structure as evidenced by the narrow GaAs and ZnSe diffraction peaks. Extensive TEM observations were made to complement the XRD measurements. Short {111}-type stacking faults were very infrequently observed in the ZnSe layers: these were considered more likely to have been caused by ion-milling damage given the known likelihood of II-VI compound semiconductors to exhibit these effects after milling.[49] Figure 14(a) shows a cross section of the entire DH structure, and there no signs of any growth defects across the field of view. Figure 14(b) is a high-resolution image showing a close-up view of the lower ZnSe/GaAs interface, as indicated by the arrow, and the exceptional crystal quality and the highly coherent interface are clearly evident.

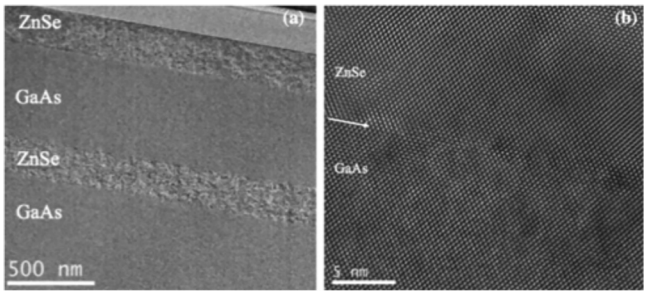

FIG. 14. (a) Cross-sectional TEM image showing ZnSe/GaAs double heterostructure; (b) High-resolution lattice image showing the lower ZnSe/GaAs interface, as indicated by the white arrow.

IV. CONCLUDING REMARKS

The epitaxial growth of II-VI/III-V heterostructures remains a challenging but worthwhile task given the potential benefits offered by these combinations of materials. In addition to some very slight differences in lattice parameters, valence mismatch and differences in thermal expansion coefficients are further factors that can negatively impact the overall crystal quality. Moreover, realizing optimum growth conditions needs to account for large differences in growth temperature as well as vapor pressures for the II-VI versus III-V constituents. More work needs to be done to investigate the impact of interfacial intermixing on the proposed behavior of nanoscale structures and superlattices, memory effect on background doping, and its impact on device performance. Our results have shown that the use of a dual-chamber MBE system with separated II-VI and III-V chambers will greatly suppress cross-contamination or unintentional doping inside the epitaxial layers. Very similar to the case for isovalent interfaces, interdiffusion is also limited at heterovalent interfaces. However, it is not very clear about the unintentional background doping level in the layers grown by the second MBE system, which has many different group-II, III, V, and VI element cells installed in the same chamber. It is worth mentioning that many physics studies of the fundamental material properties and device applications using majority-carriers, such as field-effect transistors, and even lasers, are not very sensitive to low background doping. In combination with the state-of-the-art liftoff, exfoliation, and grafting thin-film integration technologies, one can expect to further integrate these thin semiconductor epitaxial films with other lattice-mismatched substrates or layers for a basic physics study of their optical,

transport, and other quantum properties, as well as novel electronic and optoelectronic device applications, such as multicolor detectors and light emitters. We anticipate that this field will continue to grow in the foreseeable future.

ACKNOWLEDGMENTS

Much of the work described here was carried out by our students, postdocs, and collaborators at ASU and other institutions: J. J. Becker, C. M. Campbell, O. O. Cellek, W. H. G. Dettlaff, M. J. DiNezza, D. Ding, Z.-Y. He, Y. Kuo, M. Lassise, J. Lu, S. H. Lim, Z.-Y. Lin, S. Liu, D. Mohanty, R. J. Nemanich, E. Steenbergen, E. Suarez, B. D. Tracy, S. Wang, X. Wang, Y. Zhao, X.-B. Zhang, X.-H. Zhao *et al.* at ASU; X. Liu and J. K. Furdyna at Notre Dame; E. Luna and A. Trampert at Paul-Drüde Institut (Berlin); and I. Bhat and his group at RPI. The work at ASU was partially supported by a Science Foundation Arizona grant (No. SRG 0339-08) and two AFOSR grants (Nos. FA9550-10-1-0129 and FA9550-15-1-0196), an ARO MURI grant (No. W911NF-10-1-0524) and two STIR programs (Nos. W911NF1910277 and W911NF2010225), DOE EERE BAPVC programs (No. DE-EE000494), DOE EERE PVRD program (No. DE-EE0007552), and NSF/DOE QESST program (NSF CA No. EEC-1041895). The team at Notre Dame was also jointly supported by an NSF grant (No. ECCS-1002072), and the team at RPI was also supported by the BAPVC program (No. DE-EE000494). The authors gratefully acknowledge the use of the facilities at the John M. Cowley Center for High Resolution Electron Microscopy, the Center for Solid State Electronics Research (ASU NanoFab), and the Eyring Materials Center at Arizona State University.

DATA AVAILABILITY

The data that support the findings of this study are available from the corresponding author upon reasonable request.

REFERENCES

[1]Z. I. Alferov, Rev. Mod. Phys. **73**, 767 (2001); H. Kroemer, *ibid.* **73**, 783 (2001).
[2]L. Esaki and R. Tsu, IBM J. Res. Develop. **14**, 61 (1970).
[3]K. Leo, P. H. Bolivar, F. Brüggemann, R. Schwedler, and K. Köhler, Solid State Commun. **84**, 943 (1992).
[4]D. C. Tsui, H. L. Stormer, and A. C. Gossard, Phys. Rev. Lett. **48**, 1559 (1982).
[5]R. B. Laughlin, Phys. Rev. Lett. **50**, 1395 (1983).
[6]A. Y. Cho and J. R. Arthur, Prog. Solid State Chem. **10**, 157 (1975).
[7]T. Mimura, IEEE Trans. Microwave Theory Tech. **50**, 780 (2002).
[8]J. Faist, F. Capasso, D. L. Sivco, C. Sirtori, A. L. Hutchinson, and A. Y. Cho, Science **264**, 553 (1994).
[9]D. L. Smith and C. Mailhiot, J. Appl. Phys. **62**, 2545 (1987).
[10]H. Schneider and H. C. Liu, *Quantum Well Infrared Photodetectors* (Springer, New York, 2007).
[11]Y.-H. Zhang, "Heterovalent semiconductor structures and their device applications," in *Molecular Beam Epitaxy: Materials and Applications for Electronics and Optoelectronics*, 1st ed., edited by H. Asahi and Y. Horikoshi (Wiley, New York, 2019).
[12]Q. Liu, X. Zhang, L. B. Abdalla, and A. Zunger, Adv. Funct. Mater. **26**, 3259 (2016).
[13]A. Glaeser, J. Merz, R. Nahory, and M. Tamargo, IEEE Trans. Electron Devices **38**, 2720 (1991).
[14]Y. Yao, A. Alfaro-Martinez, K. J. Franz, W. O. Charles, A. Shen, M. C. Tamargo, and C. F. Gmachl, Appl. Phys. Lett. **99**, 041113 (2011).
[15]A. P. Ravikumar, T. A. Garcia, J. De Jesus, M. C. Tamargo, and C. F. Gmachl, Appl. Phys. Lett. **105**, 061113 (2014).
[16]Y. Kumagai, S. Imada, T. Baba, and M. Kobayashi, J. Cryst. Growth **323**, 132 (2011).
[17]R. L. Gunshor, M. Kobayashi, A. V. Nurmikko, and N. Otsuka, Semicond. Semimetals **33**, 337 (1991).
[18]C.-Z. Wang, D. J. Smith, S. Tobin, T. Parados, J. Zhao, Y. Chang, and S. Sivananthan, J. Vac. Sci. Technol. A **24**, 995 (2006).
[19]S. Wang, D. Ding, X. Liu, X.-B. Zhang, D. J. Smith, J. K. Furdyna, and Y.-H. Zhang, J. Cryst. Growth **311**, 2116 (2009).
[20]C. R. Li, B. K. Tanner, D. E. Ashenford, J. H. C. Hogg, and B. Lunn, J. Appl. Phys. **82**, 2281 (1997).
[21]M. P. Halsall, D. Wolverson, J. J. Davies, B. Lunn, and D. E. Ashenford, Appl. Phys. Lett. **60**, 2129 (1992).
[22]R. J. Miles, J. F. Swenberg, M. W. Wang, M. C. Phillips, and T. C. McGill, J. Cryst. Growth **138**, 523 (1994).
[23]L. Ouyang, J. Fan, S. Wang, X. Lu, Y.-H. Zhang, X. Liu, J. K. Furdyna, and D. J. Smith, J. Cryst. Growth **330**, 30 (2011).
[24]D. J. Smith, Prog. Cryst. Growth Char. Mater. **66**, 100498 (2020).
[25]J. Fan, L. Ouyang, X. Liu, J. K. Furdyna, D. J. Smith, and Y.-H. Zhang, J. Cryst. Growth **323**, 127 (2011).
[26]J. Fan, X. Liu, J. K. Furdyna, and Y.-H. Zhang, Appl. Phys. Lett. **101**, 121909 (2012).
[27]M. J. DiNezza, X.-H. Zhao, S. Liu, A. P. Kirk, and Y.-H. Zhang, Appl. Phys. Lett. **103**, 193901 (2013).
[28]S. Liu, X.-H. Zhao, C. M. Campbell, M. B. Lassise, Y. Zhao, and Y.-H. Zhang, Appl. Phys. Lett. **107**, 041120 (2015).
[29]J. Lu, M. J. DiNezza, X.-H. Zhao, S. Liu, Y.-H. Zhang, A. Kovacs, R. E. Dunin-Borkowski, and D. J. Smith, J. Cryst. Growth **439**, 99 (2016).
[30]X. Wang, C. Campbell, Y.-H. Zhang, and R. J. Nemanich, J. Vac. Sci. Technol. A **36**, 031101 (2018).
[31]M. B. Lassise, T. T. McCarthy, B. D. Tracy, D. J. Smith, and Y.-H. Zhang, J. Appl. Phys. **126**, 045708 (2019).
[32]E. Luna, A. Guzmán, A. Trampert, and G. Alvarez, Phys. Rev. Lett. **109**, 126101 (2012).
[33]H. Kim, Y. Meng, J. L. Rouviere, D. Ischeim, D. F. N. Seidman, and J.-M. Zuo, J. Appl. Phys. **113**, 103511 (2013).
[34]E. Luna, A. Trampert, J. Lu, T. Aoki, Y.-H. Zhang, M. R. McCartney, and D. J. Smith, Adv. Mater. Interfaces **7**, 1901658 (2019).
[35]X.-H. Zhao, M. J. Dinezza, S. Liu, C. M. Campbell, Y. Zhao, and Y.-H. Zhang, Appl. Phys. Lett. **105**, 252101 (2014).
[36]X.-H. Zhao, S. Liu, Y. Zhao, C. M. Campbell, M. B. Lassise, Y.-S. Kuo, and Y.-H. Zhang, IEEE J. Photovoltaics **6**, 552 (2016).
[37]X.-H. Zhao, S. Liu, C. M. Campbell, Y. Zhao, M. B. Lassise, and Y.-H. Zhang, *Proceedings of the 43rd IEEE PVSC*, Portland, OR, June 5–10, 2015 (IEEE, New York, 2016), pp. 2302–2305.
[38]Y. Zhao *et al.*, Nat. Energy **1**, 16067 (2016).
[39]T. Nakazawa, K. Takamizawa, and K. Ito, Appl. Phys. Lett. **50**, 279 (1987).
[40]J. M. Hartmann, J. Cibert, F. Kany, H. Mariette, M. Charleux, P. Alleysson, R. Langer, and G. Feuillet, J. Appl. Phys. **80**, 6257 (1996).
[41]B. Kuhn-Heinrich, W. Ossau, H. Heinke, F. Fischer, T. Litz, A. Waag, and G. Landwehr, Appl. Phys. Lett. **63**, 2932 (1993).
[42]L. W. Molenkamp and H. F. J. van't Blik, J. Appl. Phys. **64**, 4253 (1988).
[43]J. M. Olson, R. K. Ahrenkiel, D. J. Dunlavy, B. Keyes, and A. E. Kibbler, Appl. Phys. Lett. **55**, 1208 (1989).

[44]E. H. Steenbergen, M. J. DiNezza, W. H. G. Dettlaff, S. H. Lim, and Y.-H. Zhang, Appl. Phys. Lett. **97**, 161111 (2010).
[45]Z.-Y. He, C. M. Campbell, M. B. Lassise, Z.-Y. Lin, J. J. Becker, and Y.-H. Zhang, Infrared Phys. Technol. **97**, 58 (2019).
[46]O. O. Cellek, J. L. Reno, and Y.-H. Zhang, Appl. Phys. Lett. **100**, 241103 (2012).
[47]Y. Kuo, J. Becker, S. Liu, Y. Zhao, X. H. Zhao, P. Y. Su, I. Bhat, and Y.-H. Zhang, *Proceedings of the 42nd IEEE PVSC*, New Orleans, LA, June 14–19, 2015 (IEEE, New York 2015), pp. 1–6.
[48]M. B. Lassise, P. Wang, B. D. Tracy, G. Chen, D. J. Smith, and Y.-H. Zhang, J. Vac. Sci. Technol. B **36**, 02D110 (2018).
[49]A. G. Cullis, N. G. Chew, and J. L. Hutchison, Ultramicroscopy **17**, 203 (1985).